



# A hydroxyl-induced carbon nitride homojunction with functional surface for efficient photocatalytic production of H<sub>2</sub>O<sub>2</sub>



Qichao Chen <sup>a,1</sup>, Chengjie Lu <sup>a,1</sup>, Boyu Ping <sup>a</sup>, Guiyang Li <sup>a</sup>, Jiayi Chen <sup>a</sup>, ZhengMing Sun <sup>a</sup>, Yuanjian Zhang <sup>b</sup>, Qiushi Ruan <sup>a,\*</sup>, Li Tao <sup>a,\*</sup>

<sup>a</sup> Jiangsu Key Laboratory of Advanced Metallic Materials, School of Materials Science and Engineering, Southeast University, Nanjing 211189, China

<sup>b</sup> Jiangsu Engineering Laboratory of Smart Carbon-Rich Materials and Devices, Jiangsu Province Hi-Tech Key Laboratory for Bio-Medical Research, State Key Laboratory of Bioelectronics, School of Chemistry and Chemical Engineering, Southeast University, Nanjing 211189, China

## ARTICLE INFO

### Keywords:

Surface hydroxyl  
Carbon nitride homojunction  
Photocatalytic H<sub>2</sub>O<sub>2</sub> production  
Spatial charge separation  
Surface reaction kinetics

## ABSTRACT

Scalable solar-driven H<sub>2</sub>O<sub>2</sub> evolution from water holds great promise for industrial applications. Efficient H<sub>2</sub>O<sub>2</sub> generation relies on excellent spatial charge separation but simultaneously suffers from severe surface H<sub>2</sub>O<sub>2</sub> backreaction, which becomes a bottleneck for scalable H<sub>2</sub>O<sub>2</sub> evolution. Herein, a hydroxyl-induced carbon nitride (CN) homojunction coherently optimizes the bulk charge separation and suppresses surface backreaction. Surface hydroxyls provide extra electron accommodation bands for electron extraction from the bulk to the surface which are visually observed with KPFM and rationalized by DFT calculations. 2e<sup>-</sup> oxygen reduction reaction (ORR) kinetic became more favorable than 4e<sup>-</sup> ORR in the presence of hydroxyl, showing suppressed H<sub>2</sub>O<sub>2</sub> decomposition. This homojunction achieves a 4.5-fold improvement in H<sub>2</sub>O<sub>2</sub> production compared to pristine CN, and an apparent quantum yield (AQY) of 2.1 % at 500 nm in water. This work demonstrates a strategy for coherently improving spatial charge separation and surface reaction kinetics, which is applicable for various photocatalytic reactions.

## 1. Introduction

H<sub>2</sub>O<sub>2</sub> is an important strong oxidant, for a wide range of applications in chemical synthesis [1], industrial bleaching [2], and fuel cells [3]. While more than 95 % of H<sub>2</sub>O<sub>2</sub> is synthesized through the anthraquinone oxidation process that causes a huge energy consumption and water pollution [4], there is a strong demand for eco-friendly production of H<sub>2</sub>O<sub>2</sub> to save resources. Photocatalytic H<sub>2</sub>O<sub>2</sub> production from water shows great potential in practical use since this eco-friendly process is driven by inexhaustible solar energy. [5–9] As a benchmark metal-free photocatalyst for water splitting, CO<sub>2</sub> reduction, and pollutant degradation [10–13]. Carbon nitride (CN) is also considered to be one of the most promising photocatalysts for H<sub>2</sub>O<sub>2</sub> production benefiting from its suitable band structure, chemical stability, environmental friendliness and earth abundance. [14].

Compared with TiO<sub>2</sub>, ZnO, BiVO<sub>4</sub>, and other photocatalysts, CN has a tunable band structure to realize the photocatalytic conversion of water to H<sub>2</sub>O<sub>2</sub> by visible light [5,6,8,10,11]. Shiraishi et al. [14,15] firstly

confirmed CN is highly selective for the oxygen reduction reaction (ORR) to H<sub>2</sub>O<sub>2</sub> due to the efficient formation of 1,4-endoperoxide species on its surface. Recently, CN exhibited significantly enhanced performance in the field of photocatalytic synthesis of H<sub>2</sub>O<sub>2</sub>. For instance, Choi et al. [16] reported promoted electron trapping and interlayer charge separation on doped polymeric CN, showing excellent selectivity toward the H<sub>2</sub>O<sub>2</sub> production with a sacrificial agent. Ohno et al. [17] atomically dispersed Sb on CN photocatalyst to notably promoting two-electron ORR by forming  $\mu$ -peroxide at the single-atom sites, achieving a new benchmark AQY of 17.6 % at 420 nm and about 7 % at 450 nm for photocatalytic H<sub>2</sub>O<sub>2</sub> production in pure water. However, the accumulation of continuously generated H<sub>2</sub>O<sub>2</sub> suffers from back reaction through surface states, which is a bottleneck for further improving the efficiency. Since the efficiency of H<sub>2</sub>O<sub>2</sub> production relies on efficient spatial charge separation and suppressed H<sub>2</sub>O<sub>2</sub> back reaction, a synergistic strategy for promoting photo-generated charge separation for two-electron ORR and suppressing back reaction via surface engineering is highly demanded for efficient H<sub>2</sub>O<sub>2</sub> photosynthesis.

\* Corresponding authors.

E-mail addresses: [ruanqs@seu.edu.cn](mailto:ruanqs@seu.edu.cn) (Q. Ruan), [tao@seu.edu.cn](mailto:tao@seu.edu.cn) (L. Tao).

<sup>1</sup> Qichao Chen, Chengjie Lu contributed equally to this work.

Strategies for separating photo-generated charges include introducing specific defects [18,19], loading noble metal nanoparticles [20, 21], constructing heterojunction etc., among which constructing heterojunction is the most prominent method since the interfacial electric field provides strong driving force for directional carriers transport [22–26]. Nevertheless, Schottky barrier and abundant defects will form at the CN heterojunction interface due to mismatched lattice constants and Fermi energy levels of two components, which unavoidably impedes the transfer of photo-generated charges and weakens improvement effect [27–30]. A CN homojunction outperforms a heterojunction in charge separation, because the continuously changed band structure and well-matched lattice can minimize the resistance of photo-generated charges transfer at interface during photocatalysis [26, 27,31]. Although, most homojunctions own facilitated charge separation, their sluggish surface reaction kinetics have not been improved effectively. A flexible design of surface terminals may mitigate competitive reverse reaction of  $\text{H}_2\text{O}_2$  decomposition on CN surface, such as utilizing surface hydroxide radical to capture excess electrons or designing iodide ions terminal to improve the selectivity of  $2\text{e}^-$  ORR [32, 33], but these strategies are difficult to be compatible with the construction of homojunction.

In this work, we developed a hydroxyl-induced CN homojunction (homo-CN) composing a hydroxyl-rich CN (HR-CN) nanolayer in-situ grown on hydroxyl-deficient CN (HD-CN) nanosheets. The variation in hydroxyl concentration on CN samples tuned their band structures, forming a gradient driving force for electron-hole separation, doubling photo-generated charge lifetime to 24.3 ns and extending light absorption edge to about 500 nm. Kinetically, surface hydroxyls provide extra electron accommodation bands for efficient electron extraction from the bulk to the surface, and suppress  $\text{H}_2\text{O}_2$  back reaction on surface by enhancing the absorption energy of  $^{\bullet}\text{OOH}$  (the intermediate species to form the final products of  $\text{H}_2\text{O}_2$ ) and increasing the overpotential for the  $4\text{e}^-$  ORR. Benefiting from facilitated surface kinetics, the CN homojunction exhibits significantly enhanced photocatalytic performance for  $\text{H}_2\text{O}_2$  production with a 2.1 % AQY at 500 nm, which is among the highest reported in pure water. This work demonstrates a facile strategy for coherently improving spatial charge separation and surface reaction kinetics, that can be applied to various photosynthesis processes.

## 2. Experimental section

### 2.1. Preparation of HD-CN and HR-CN photocatalysts

An oxygen-deficient precursor “dicyandiamide ( $\text{C}_2\text{H}_4\text{N}_4$ )” was used to prepare HD-CN and an oxygen-rich precursor “urea ( $\text{CH}_4\text{N}_2\text{O}$ )” was used to prepare HR-CN. Typically, 2 g dicyandiamide ( $\text{C}_2\text{H}_4\text{N}_4$ , 99 %, Aladdin) mixed with 10 g ammonium chloride ( $\text{NH}_4\text{Cl}$ , 99.5 %, Macklin), or 2 g urea ( $\text{CH}_4\text{N}_2\text{O}$ , 98 %, Aladdin) were placed into an  $\text{Al}_2\text{O}_3$  crucible with a cover and annealed at 520 °C for 4 h with a ramp rate of 10 °C min<sup>-1</sup> in a tube furnace (TL-1200X). During the calcination process, the pressure in the tube furnace was kept at 0.5 torr and the atmosphere was high purity argon (>99.5 %). According to the precursors, the obtained products were named as HD-CN (precursor: dicyandiamide+ ammonium chloride) and HR-CN (precursor: urea). The preparation process of bulk CN is the same as HD-CN, without adding ammonium chloride.

### 2.2. Preparation of the homojunction

200 mg HD-CN was dispersed in 50 mL ethanol ( $\text{C}_2\text{H}_5\text{OH}$ , 99.6 %, Aladdin) by sonification for 10 min, after which urea was dissolved in the dispersion. The dispersion was kept in a water bath at 75 °C and stirred until it was crystallized. Then the obtained powder was placed into a tube furnace to annealed at 520 °C for 2 h with a ramp rate of 10 °C min<sup>-1</sup> under an Argon atmosphere. In such a way, a HR-CN nanolayer was deposited on the surface of HD-CN, so that the CN

homojunction was constructed. According to the weight percentage of added urea in precursor, the final products were named as homo-CN0 %, homo-CN1.25 %, homo-CN5 %, homo-CN10 % and homo-CN15 %, among which the best sample (homo-CN5 %) was simply labelled as homo-CN in the manuscript.

### 2.3. Materials characterization

Scanning electron microscopy (SEM, Sirion) and transmission electron microscope (TEM, Talos F200X) were employed to characterize the morphology of samples. The elemental distribution of the samples was provided by an energy dispersion X-ray (EDX) spectrometer attached to TEM. The X-ray diffraction (XRD, Smartlab-3) was used to measure the phase structures of the samples at the scanning angles 2θ from 10° to 80°. The chemical functional groups of samples were determined by Fourier transform infrared spectroscopy (FT-IR, Nicolet 5700). Elemental analysis (Thermo Fisher) was used to determine the C, N, O and H contents of samples. Solid-state <sup>13</sup>C MAS NMR spectra were taken on a Bruker Advance III HD 400 MHz. UV-vis diffuse reflectance spectrum (DRS) of photocatalysts was measured by a Shimadzu UV-2600 spectrometer equipped with an integrating ball. The Brunauer-Emmett-Teller (BET, ASAP 2020) surface area was calculated according to the nitrogen adsorption desorption isotherm and the Barrett-Joyner-Halenda (BJH) was used to obtain the pore size distribution of samples through adsorption isotherm branch. The X-ray photoelectron microscope (XPS, PHI 500) was used for determining the precise chemical constitution of samples. Surface photovoltage measurements were operated by Kelvin Probe Force Microscopy (KPFM) in tapping mode, which sequentially recorded the topography and surface potential of test samples. The photoluminescence (PL) spectrum was analyzed with a Shimadzu RF-5301 instrument at room temperature using a fluorescence spectrophotometer at an excitation wavelength of 380 nm. Transient-state PL spectra were recorded with a single photon counting spectrometer from (Edinburgh Instrument, FLS 980) with 1 μs pulse lamp as the excitation. The average lifetime is calculated by the following equation:  $\tau_{\text{AVE}} = [\tau_1\text{A}_{12} + \tau_2\text{A}_{22} + \tau_3\text{A}_{32}] / [\tau_1\text{A}_{12} + \tau_2\text{A}_{22} + \tau_3\text{A}_{32}]$ . The reactive oxygen species (ROS) was investigated by the spin trapping-EPR tests at room temperature. DMPO was used as a spin trapping reagent to detect  $\bullet\text{O}_2^-$ . The measurements were conducted as follows: catalysts (1 mg) were dispersed in aqueous solutions (500 μL) containing DMPO (0.1 mmol) with a 2 mL quartz bottle, which was sealed with a rubber septum cap. After short ultrasonication for 5 min, a Xe lamp ( $\lambda > 400$  nm) was used as the light source.

### 2.4. Measurement of photocatalytic activities

The production process of  $\text{H}_2\text{O}_2$  was described below: 50 mg photocatalyst was dispersed in 50 mL 10 % ethanol solution for half-reaction test and in 50 mL deionized water for overall reaction. The photocatalytic reaction occurred under the visible light (300 W xenon lamp,  $\geq 420$  nm, PLS-SXE300D, light intensity  $314 \pm 5$  mW/cm<sup>2</sup>). The concentration of  $\text{H}_2\text{O}_2$  is measured by iodometry [39].

The AQY of the photocatalytic reaction was measured under the illumination of a Xenon lamp (Newport 150 W) equipped with bandpass filters (FWHM:  $10 \pm 2$  nm) of 360 nm, 420 nm, 450 nm and 500 nm. Typically, 50 mg of the catalyst was dispersed into 50 mL of a 10 vol% ethanol solution or deionized water, and then sonicated for 5 min. Subsequently, the reactor was placed at a distance of 10 cm from the filter to perform the AQY experiment. At the same time, the intensity of the light was measured (0.78 mW/cm<sup>2</sup> for 360 nm, 1.54 mW/cm<sup>2</sup> for 420 nm, 2.08 mW/cm<sup>2</sup> for 450 nm and 2.28 mW/cm<sup>2</sup> for 500 nm). During the photocatalytic experiment, the irradiation area was 2.28 cm<sup>2</sup>. After 60 min, the absorption curve of mixed solution was detected by UV-vis spectroscopy, and the corresponding relationship between the absorption peak and the concentration of the  $\text{H}_2\text{O}_2$  solution was obtained.

The AQY value was calculated according to the following Equation:

$$\eta_{AQY} = \frac{N_e}{N_p} \times 100\% = \frac{2 \times n \times N_A}{E_{\text{total}}} \times 100\%$$

$$= \frac{2 \times n \times N_A}{S \times P \times t \times \lambda} \times 100\% = \frac{2 \times n \times N_A \times h \times c}{S \times P \times t \times \lambda} \times 100\%$$

Where,  $n$  is the amount of  $\text{H}_2\text{O}_2$  molecules (mol),  $N_A$  is Avogadro constant ( $6.022 \times 10^{23}$  /mol),  $h$  is the Planck constant ( $6.626 \times 10^{-34}$  JS),  $c$  is the speed of light ( $3 \times 10^8$  m/s),  $S$  is the irradiation area ( $\text{cm}^2$ ),  $P$  is the intensity of irradiation light ( $\text{W}/\text{cm}^2$ ),  $t$  is the photoreaction time (s),  $\lambda$  is the wavelength of the monochromatic light (m).

The working curve for determining the concentration of  $\text{H}_2\text{O}_2$  was established and the corresponding precision  $R^2$  is 0.996.

## 2.5. Isotope labeling measurements with $\text{H}_2\text{O}^{18}$

30 mg of homo-CN and 10 mL of  $\text{H}_2\text{O}^{18}$  (20 %) were added in a hermetic quartz bottle (20 mL) under sonication for 5 min. Afterward, the bottle was sealed entirely and irradiated by visible light ( $\lambda > 420$  nm). After 1 h irradiation, 1 mL of suspension was extracted and mixed with 1 mL solutions containing luminol (100  $\mu\text{mol}/\text{L}$ ) and horseradish peroxidase (HRP, 50  $\mu\text{g}/\text{mL}$ ). It proved that the photo-generated  $\text{H}_2\text{O}_2$  reacted with luminol in the presence of HRP and formed Lunimol-Ox, which was analyzed by liquid chromatography-mass spectrometry.

## 2.6. Photoelectrochemical performance

The instantaneous photocurrent responses were measured under the visible light and the electrochemical impedance spectrum (EIS) was performed under open-circuit voltage with a frequency range of 100 kHz–10 mHz by using an electrochemical workstation (CHI660E, Shanghai, China). An Ag/AgCl electrode and a Pt foil were used as the reference electrode and counter electrode respectively. The working electrodes were prepared by binding catalyst powder onto an ITO glass. By simple sonication, 5 mg photocatalyst was dispersed in 2 mL N,N-Dimethylformamide containing 20  $\mu\text{L}$  Nafion. Then, 40  $\mu\text{L}$  of the above suspension was dropped to the single-side conductive ITO glass ( $20 \times 2.1 \text{ mm}^2$ ,  $10 \Omega \cdot \text{sq}^{-1}$ ) within an area of  $1 \times 1 \text{ cm}^2$  and subsequently dried completely.

## 2.7. DFT simulation

The modeling in this work was performed in the framework of the Density Functional Theory (DFT) as implemented in the Vienna *Ab initio* Simulation Package (VASP). For better understanding the influence of terminal species (-NH<sub>2</sub>, -OH) on the electronic properties of carbon nitride, a single-layer fragment with three tri-oxazine units was adopted as the investigating CN substrate. The projector augmented wave method (PAW) together with the generalized gradient approximation (GGA) for the exchange-correlation energy functional constructed by Perdew-Burke-Ernzerhof (PBE) was adopted. Thereafter, the geometrical optimization as well as the electronic computation was conducted using a cutoff energy of 480 eV and a Monkhorst-Pack mesh with the total number of the  $k$ -points up to 50.

## 3. Results and discussion

### 3.1. Characterizations of the hydroxyl-induced homojunction

A variety of CN structures are prepared and verified by XRD in Fig. S1. All samples exhibit two diffraction peaks of CN around 13.2° and 27.4°. These peaks correspond to in-plane repeat tri-s-triazine units and interlayer stacking reflection, respectively [37]. The (002) peaks of

HD-CN and homo-CN shift to a lower degree of 27.2°, which indicates increased stacking distance between interlayers in these two samples [23]. The full width at half maximum (FWHM) of (002) peak of HD-CN is 2.53° that is broader than that of HR-CN (1.87°), representing its decreased crystallinity. The even broader (002) peak of homo-CN (2.89°) is probably due to the in situ formation of homojunction with disordered lattice at interface [28].

SEM images clarify the formation of CN homojunction as shown in Fig. S2 and Fig. S3. The morphology of HD-CN (Fig. S3a) is similar to previously reported CN nanosheets with generally compact and continuous surface [38]. After the homojunction has been constructed, homo-CN exhibits a slightly aggregated structure and a loose meshed surface, as shown in the inset of Fig. S2. This loose surface differs from bulk CN (Fig. S3b) but is similar to HR-CN (Fig. S3c). Thus, HR-CN covers the surface of HD-CN to form the homojunction after the second annealing process. While without growing HR-CN nanolayer (homo-CN0 %, Fig. S3d), HD-CN agglomerate seriously. The results of nitrogen adsorption-desorption in Table S1 and Fig. S4 show that the specific surface area of homo-CN ( $50.8 \text{ m}^2 \cdot \text{g}^{-1}$ ) is much higher than homo-CN0 % ( $9.1 \text{ m}^2 \cdot \text{g}^{-1}$ ), confirming the lower aggregation degree of homo-CN.

TEM images provide direct observation of CN homojunction interface. The high-resolution TEM image of homo-CN (Fig. 1a) shows that two phases can be found at the edge of homo-CN. The darker part on the left in Fig. 1a is CN nanosheet covered by CN nanolayer, and an obvious boundary can be observed which is assigned to HR-CN. Distinct lattice fringes with similar lattice distance (0.34 nm) can be observed in both phases, but there are several nm-thick disordered regions between these two phases, corresponding to the homojunction interface. While for HD-CN, only one homogeneous phase with a clear boundary and lattice fringe can be observed (interlayer distance of 0.34 nm, Fig. S5). Furthermore, the EDS spectrum (Fig. S6) confirms that both two phases are composed of C, N and O elements.

According to the relative peak intensities of different samples in FT-IR spectrum (Fig. 1b), HR-CN exhibits more prominent tertiary nitrogen C-N stretching ( $1408 \text{ cm}^{-1}$ ) and conjugated CN stretching ( $1640 \text{ cm}^{-1}$ ) than HD-CN, suggesting its higher polymerization degree [36]. Similar to HD-CN, homo-CN shows relatively low intensity peaks at  $1406 \text{ cm}^{-1}$  and  $1640 \text{ cm}^{-1}$ , indicating its low polymerization degree as also evidenced in Fig. S1. It confirms that the bulk property of HD-CN dominates in homo-CN sample since the HR-CN precursor amount is as low as 5 %. Remarkably, HR-CN shows a significant peak corresponding to hydroxyl groups on CN surface at  $3500 \text{ cm}^{-1}$ , which is almost preserved in homo-CN sample. This suggests that the surface property of homo-CN is similar to HR-CN with a hydroxyl-rich surface after the formation of the homojunction [34,35]. Furthermore, solid-state <sup>13</sup>C NMR of samples (Fig. 1c) all exhibit two strong peaks at 156.6 and 164.2 ppm, corresponding to the chemical shifts of  $\text{C}_{3\text{N}}$  and  $\text{C}_{2\text{N-NH}_2}$  in the heptazine units. While for HR-CN and homo-CN, there is an additional weak peak appears at around 130 ppm, which can be assigned to the  $\text{C}_{2\text{N-OH}}$  [39]. Quantitatively, according to the elemental analysis in Table 1, HR-CN shows the highest content of oxygen (12.34 wt%) due to its hydroxyl-rich surface. Oxygen element concentration in HD-CN (6.21 wt%) is only half of HR-CN. In-situ growing a small amount of HR-CN on HD-CN achieves an oxygen concentration of 7.30 wt% for homo-CN. Moreover, hydrogen percentages of HR-CN (2.46 wt%) and homo-CN (2.37 wt%) are lower than HD-CN (3.02 wt%), due to substitution of surface amino terminals with hydroxyl groups. The introduction of hydroxyl groups is also confirmed by XPS as shown Fig. S7. In O1s spectra (Fig. S7b), two peaks that can be determined for all samples, the peak located at 531.1 eV can be attributed to the O-H bonds while the weak peak at 532.3 eV represents the absorbed water [32]. HR-CN and homo-CN have a larger peak area at 531.1 eV which indicates their abundant hydroxyl groups. In the C1s spectra of HD-CN, HR-CN and homo-CN (Fig. S7c), apart from the typical peaks at 284.6 eV [ $\text{C}=\text{C}$ ] and 288.3 eV [ $\text{N}=\text{C-N}$ ], HR-CN and homo-CN have an

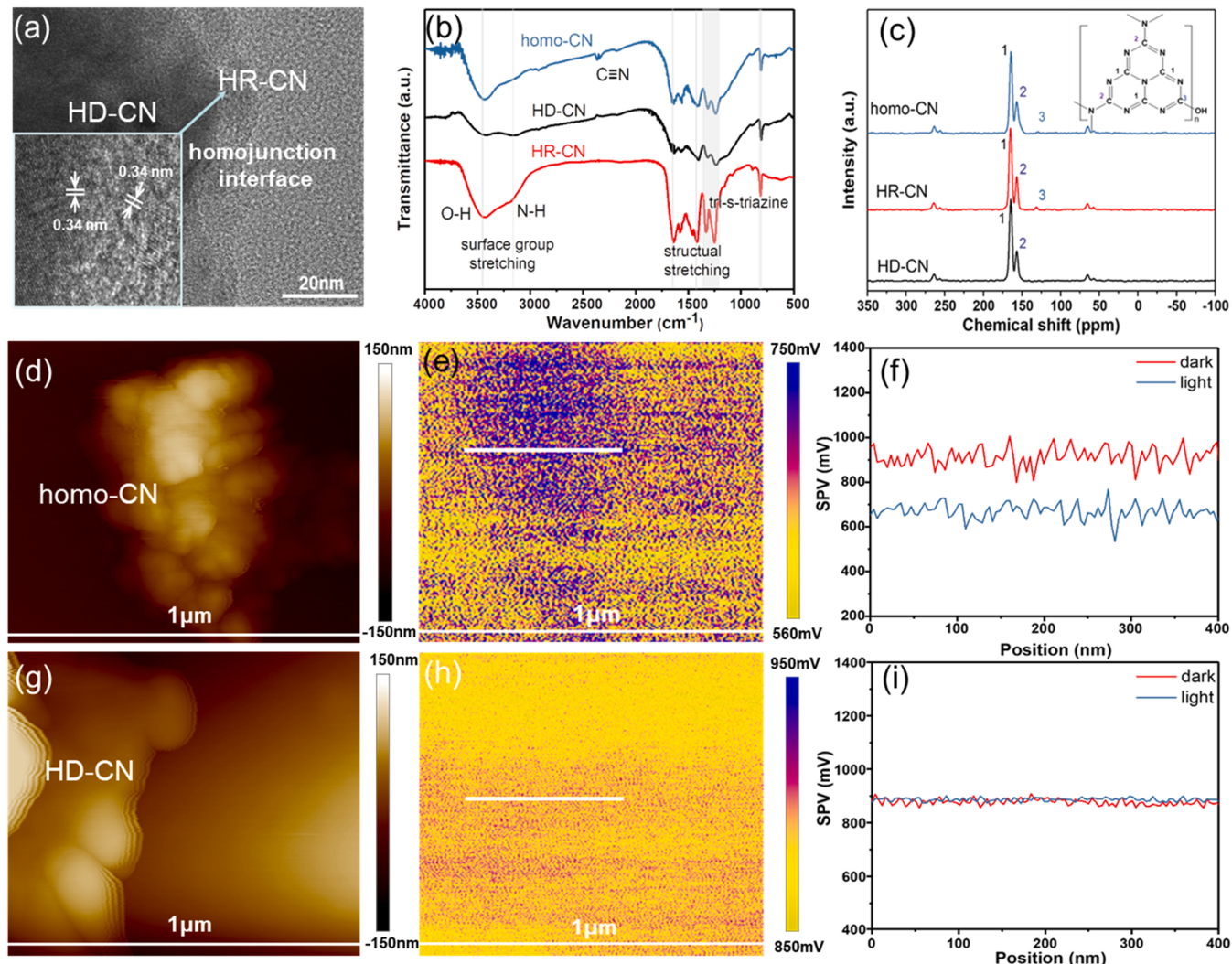


**Fig. 1.** (a) TEM images of homo-CN; (b) FT-IR spectroscopy of homo-CN, HD-CN and HR-CN. (representative peaks around  $810\text{ cm}^{-1}$ ,  $1200\text{--}1700\text{ cm}^{-1}$ ,  $2885\text{--}3325\text{ cm}^{-1}$  and  $3400\text{--}3600\text{ cm}^{-1}$  can be assigned to the breathing mode of tri-s-triazine units, aromatics stretching modes of heterocycle, stretches of N-H and O-H groups [34,35]. The bands between  $1204$  and  $1316\text{ cm}^{-1}$  are assigned to secondary bridging nitrogen, while the peak at  $1408\text{ cm}^{-1}$  associating with C-N stretching of tertiary nitrogen atoms. The band at  $1640\text{ cm}^{-1}$  corresponds to conjugated CN stretching) [36]. (c) Solid-state  $^{13}\text{C}$  MAS NMR of HD-CN, HR-CN and homo-CN. (d-f) AFM height image, surface potential mapping under light and line profiles of the surface photovoltaic (SPV) (potential difference under light and in the dark) of homo-CN; (g-i) AFM height image, surface potential mapping under light and line profiles of the SPV of HD-CN characterized by KPFM.

**Table 1**  
Elemental analysis of HD-CN, HR-CN and homo-CN.

Sample	N (wt%)	C (wt%)	O (wt%)	H (wt%)
HD-CN	55.49	33.14	6.21	3.02
HR-CN	51.12	32.27	12.34	2.46
homo-CN	55.01	33.59	7.30	2.37

enhanced peak at  $286.4\text{ eV}$  which corresponds to C-OH [39]. The N1s spectra of samples also can be divided into three peaks at  $398.7\text{ eV}$ ,  $399.8\text{ eV}$  and  $400.8\text{ eV}$ , which correspond to the C=N=C, N-(C)3 and C-NH groups. While for HR-CN and homo-CN, the C-NH peaks exhibit a weaker intensity than HD-CN, indicates the terminal  $-\text{NH}_2$  of HR-CN and homo-CN is partly replaced by hydroxyl group. Therefore, it can be concluded that a hydroxyl-induced CN homojunction is formed.

KPFM enables nanometer-scale imaging of the surface potential change on the hydroxyl-induced homojunction under irradiation and in the dark (surface potential mapping of homo-CN and HD-CN in the dark are supplemented in Fig. S8a and b) [40]. The AFM height images of homo-CN and HD-CN particles are shown in Fig. 1d and g, respectively.

When homo-CN is irradiated, a rough outline of sample similar to the AFM image (Fig. 1d) can be observed through SPV mapping in Fig. 1e. According to the SPV profiles in Fig. 1f, homo-CN obtains a negative SPV signals (about  $300\text{ mV}$  lower than that in dark) under irradiation, suggesting the accumulating of photoelectrons on the surface of homo-CN. This phenomenon is not caused by substrate since bare substrate shows negligible SPV difference between dark and light (Fig. S9) [40]. The hydroxyl-rich surface of homojunction clearly affects the spatial charge distribution by extracting the photoelectrons to the surface. A control experiment conducted on HD-CN is shown in Fig. 1g-i. Under irradiation, almost no surface potential difference can be observed between HD-CN and substrate (Fig. 1h) and negligible SPV (less than  $20\text{ mV}$ ) is observed on HD-CN (Fig. 1i), suggesting its poor charge separation ability. Conclusively, the successfully synthesized hydroxyl-induced homojunction enabled efficient spatial charge separation under illumination, and photoelectrons were efficiently extracted from the bulk to the surface through hydroxyl groups.

### 3.2. Photocatalytic performance of $H_2O_2$ production

To explore the effect of homojunction on the photocatalytic production of  $H_2O_2$ , activity of HD-CN, HR-CN and homo-CN are evaluated under visible light. As shown in Fig. 2a, after 1 h reaction, HD-CN obtains a higher  $H_2O_2$  yield (173.7  $\mu\text{M}$ ) than HR-CN (77.5  $\mu\text{M}$ ), and homo-CN has the highest yield of 508.4  $\mu\text{M}$ , which is 2.9 and 6.6 times higher than HD-CN and HR-CN respectively. Moreover, homo-CN exhibits favorable photocatalytic performance stability since its  $H_2O_2$  yield remains 87.5 % of the first run after 5 reaction cycles (Fig. S10). Fig. S11 shows the effect of HR-CN content on the  $H_2O_2$  production performance of the samples. In general, all samples with homojunction obtain higher  $H_2O_2$  yield than HD-CN, and homo-CN has the highest production rate which is 4.5 times higher than HD-CN after a 2 h reaction. The improved  $H_2O_2$  yield is caused by formation of homojunction rather than the secondary annealing because the  $H_2O_2$  yield of homo-CN0 % is even lower than bulk DCN.

To further determine the  $H_2O_2$  synthesis process of samples, photocatalytic reactions are carried out under different conditions for 2 h. As shown in Fig. 2b, homo-CN also possesses 177  $\mu\text{M}$  of  $H_2O_2$  yield in pure water, while HD-CN and HR-CN almost have no yield. When benzoquinone (BQ) acts as a  $\text{O}_2^-$  capture agents in the reaction system, all the samples show that  $H_2O_2$  yields reduced by more than 95 %. This phenomenon confirms that these samples synthesize  $H_2O_2$  through a two-step single-electron reduction route, during which the  $\text{O}_2^-$  is a necessary intermediate product, as shown in Eqs. (1)–(4) [41,42]. This result is consistent with the EPR spectra of homo-CN (Fig. 2c), as a strong signal of DMPO- $\text{O}_2^-$  is detected after homo-CN is irradiated. When electrons in the reaction system are captured by  $\text{AgNO}_3$ , few  $H_2O_2$  is produced by homo-CN (less than 20  $\mu\text{M}$ ), indicating that most  $H_2O_2$  came from the ORR reaction and the oxidation reaction is oxygen evolution. The  $\text{O}_2$  evolution activity of samples is also measured by investigating concentration of dissolved oxygen, homo-CN (94.3  $\mu\text{M}$ ) and HR-CN

(83.5  $\mu\text{M}$ ) have a higher activity than HD-CN (44.2  $\mu\text{M}$ ), indicating their better oxidation ability of photo-holes. The  $\text{H}_2\text{O}^{18}$  isotope experiments directly confirm that the  $\text{O}_2$  generated by photo-holes of homo-CN is reduced to  $H_2O_2$ . As shown in the Fig. 2d, isotope luminol oxide- $\text{O}^{18}$  (around 182  $m/z$ ) peak is detected when adding luminol solution and HRP into the homo-CN suspension (after 2 h illumination), while the reference sample (125  $\mu\text{M}$   $H_2O_2$ ) only shows the luminol oxide- $\text{O}^{16}$  peak ( $m/z = 180$ ) [43].



The wavelength dependence of the  $H_2O_2$  generation efficiency is measured under the illumination of light source equipped with band pass filters ( $\lambda = 360, 420, 450$  and 500 nm), as shown in Fig. 2e. The AQY of homo-CN exhibits similar light wavelength dependence with absorbance. homo-CN shows a high AQY of 27.7 % at 360 nm and 25.7 % at 420 nm. Moreover, homo-CN still has the AQY of 5.6 % at 450 nm and 3.8 % at 500 nm. Notably, when there is no sacrificial reagent in the reaction system, homo-CN exhibits an AQY of  $2.6 \pm 0.1$  % at 450 nm and  $2.1 \pm 0.07$  % at 500 nm respectively which is comparable to most efficient CN based photocatalysts at such a long wavelength as shown in Table S3. Further, the solar-to-chemical conversion (SCC) efficiency of homo-CN is also determined to be 0.19 % under one-sun illumination without any sacrificial agent detailed in Table S2, and depicted in Fig. S12. We extract the charge separation efficiency ( $\epsilon_{\text{cs}}$ ) of CN homojunction from its AQY results in Fig. 2e and investigated its dependence on wavelength (the incident photons energy) in Fig. 2f. Assuming photo-generated electrons are fully utilized when holes are removed by

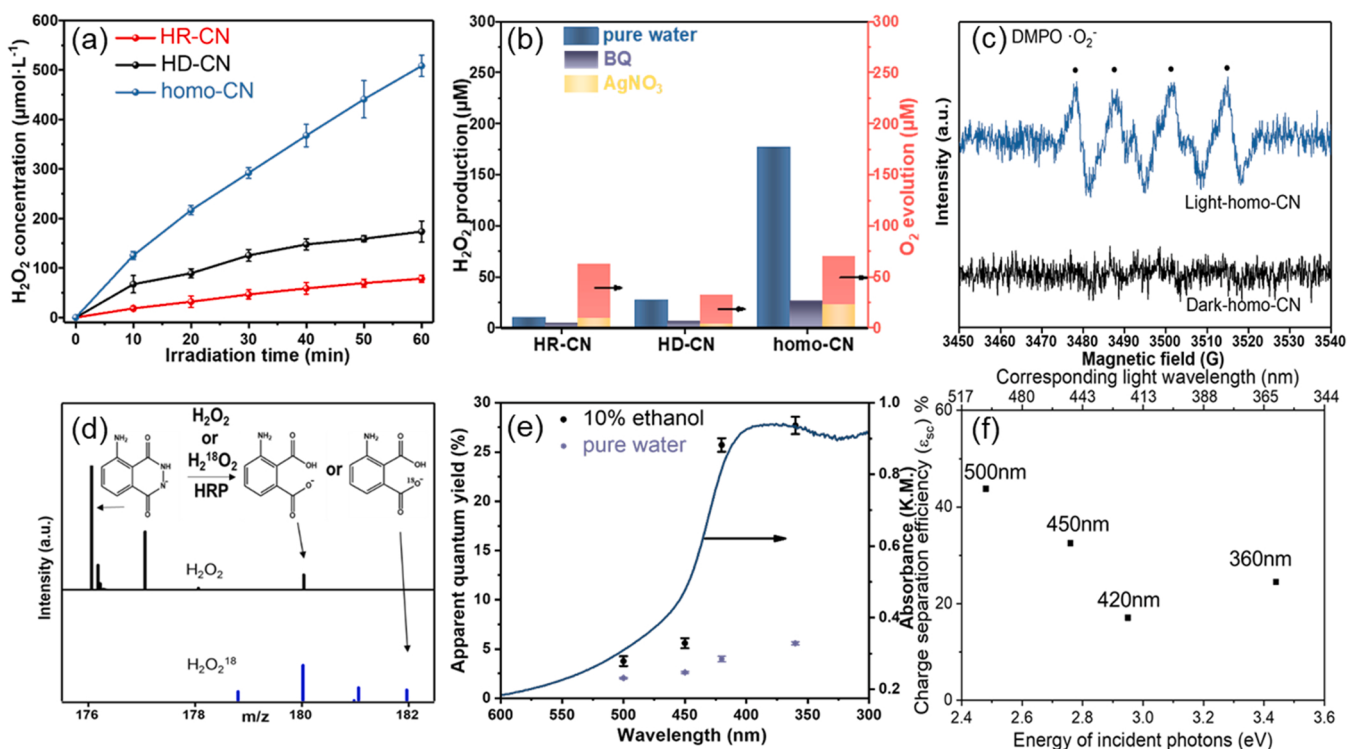


**Fig. 2.** (a) The  $H_2O_2$  yield of HR-CN, HD-CN and homo-CN (1 mg/mL) with 10 % ethanol; (b)  $H_2O_2$  yield of HD-CN, HR-CN and homo-CN (50 mg suspended in 50 mL water) after 2 h photocatalytic reaction under different conditions ( $O_2$  evolution is also measured when  $\text{AgNO}_3$  is added); (c) EPR signal of DMPO- $\text{O}_2^-$  of homo-CN; (d) mass spectra of luminol before and after oxidation with hydrogen peroxide generated by photocatalytic  $H_2^{18}\text{O}$  splitting; (e) absorbance and AQY of homo-CN; (f) charge separation efficiency ( $\epsilon_{\text{cs}}$ ) of homo-CN sample under monochromatic light with different wavelength (photon energy).

scavenger, the  $\varepsilon_{\text{cs}}$  (the ratio between AQY measured without and with hole scavenger) is defined as the photo-generated charge separation efficiency for  $\text{H}_2\text{O}_2$  production. The corresponding charge separation efficiency at this wavelength (500 nm) is 54.4 % while shorter wavelength or higher photon energy leads to a charge separation efficiency of 46.9 % at 450 nm, 15.6 % at 420 nm and 17.1 % at 360 nm. Therefore, the homojunction exhibited a remarkably higher charge separation efficiency than a single material for charges with low energy.

### 3.3. Charge excitation and separation due to band alignment over homojunction

To witness the significant difference in the charge separation of this hydroxyl-induced homojunction, steady state and transient PL are measured. As shown in Fig. 3a, the steady state PL intensity of homo-CN is weaker than HD-CN and HR-CN, suggesting the improved charge separation of photo-induced electron-hole pairs. The red shift of the homo-CN PL peak suggests its narrower bandgap. Remarkably, homo-CN homojunction exhibits a long fluorescent lifetime of 24.3 ns which is 2-time of HD-CN (11.7 ns) and 3-time of HR-CN (7.5 ns) in Fig. 3b. The prolonged radiative charge recombination process is due to the indirect charge travel across the homojunction [16,44].

To explain the superior AQY at long wavelength, UV-vis DRS is employed to survey the optical absorption of different samples. As displayed in Fig. 3c, the absorption edges of HR-CN and HD-CN are around 450 nm while the homojunction extends the optical absorption edge to about 500 nm (the main absorption peaks). Thus, homo-CN has better visible light-harvesting ability that is beneficial to photocatalytic  $\text{H}_2\text{O}_2$  production. In addition, homo-CN and HR-CN show weak absorption peaks around 450–500 nm, suggesting that the  $n \rightarrow \pi^*$  electron transition of the lone pair electrons is caused by surface states such as hydroxyl groups [45,46].

The bandgaps of samples are calculated by Kubelka-Munk function according to their optical absorption spectrum. It can be found in the insert of Fig. 3c that HD-CN and HR-CN have relatively wider bandgaps

than homo-CN (2.51 eV), and the bandgap of HR-CN (2.75 eV) is larger than HD-CN (2.66 eV). The reduced bandgap of homojunction sample is because electrons are directly promoted from the valence band of HD-CN to the conduction band of HR-CN at the homojunction interface [47,48]. This effect is most pronounced when the HR-CN content is 5 % as shown in Fig. S13. When HD-CN has been fully covered by HR-CN, the excessive HR-CN will not influence the homojunction interface, but dominates the light absorption property. Therefore, homo-CN shows a narrower bandgap than that of homo-CN1.25 % (2.60 eV) and homo-CN15 % (2.63 eV).

In addition, the flat-band potential ( $E_{\text{FB}}$ ) of HD-CN, HR-CN and homo-CN are estimated from Mott-Schottky plots (Fig. 3d and S14). All the samples show a characteristic of n-type and the  $E_{\text{FB}}$  of samples tested by Mott-Schottky plots is approximately equal to their conduction band potentials [49]. Thus, the conduction band potentials of HD-CN, HR-CN and homo-CN is determined to be  $-1.12\text{ V}$ ,  $-0.97\text{ V}$  and  $-0.97\text{ V}$  (vs. RHE,  $\text{pH} = 7$ ), respectively. Moreover, the relative difference in the valence band positions between HD-CN and homo-CN (0.24 eV) obtained from VB-XPS (Fig. 3e) is consistent with the results calculated from UV-vis DRS and Mott-Schottky plots. The band structure of samples is shown in Fig. 3f, all samples have more negative conduction band (CB) potentials than that required for reducing  $\text{O}_2$  to  $\text{O}_2^-$ . Although homo-CN has photo-generated electrons with weaker reducing ability than HD-CN, its  $\text{H}_2\text{O}_2$  yield is significantly higher. Hence, it can be concluded that the lower charge recombination rate and prolonged charge lifetime boost the photocatalytic production of  $\text{H}_2\text{O}_2$ .

To further characterize the transport and separation capabilities of photo-generated carriers, EIS measurement and transient photocurrent response are conducted. As shown in Fig. S15a, homo-CN exhibits smaller semicircle radii of the Nyquist plot than HD-CN and HR-CN, which represents its higher efficiency on charge separation and transport [50]. In addition, the equivalent circuit data fitted from EIS measurement is shown in Table S4. The homo-CN has the lowest  $R_{\text{ct}}$  ( $8498\text{ ohm}\cdot\text{cm}^{-2}$ ) corresponding to its highest conductivity. According to Fig. S15b, the transient photocurrent responses of sample sequences of

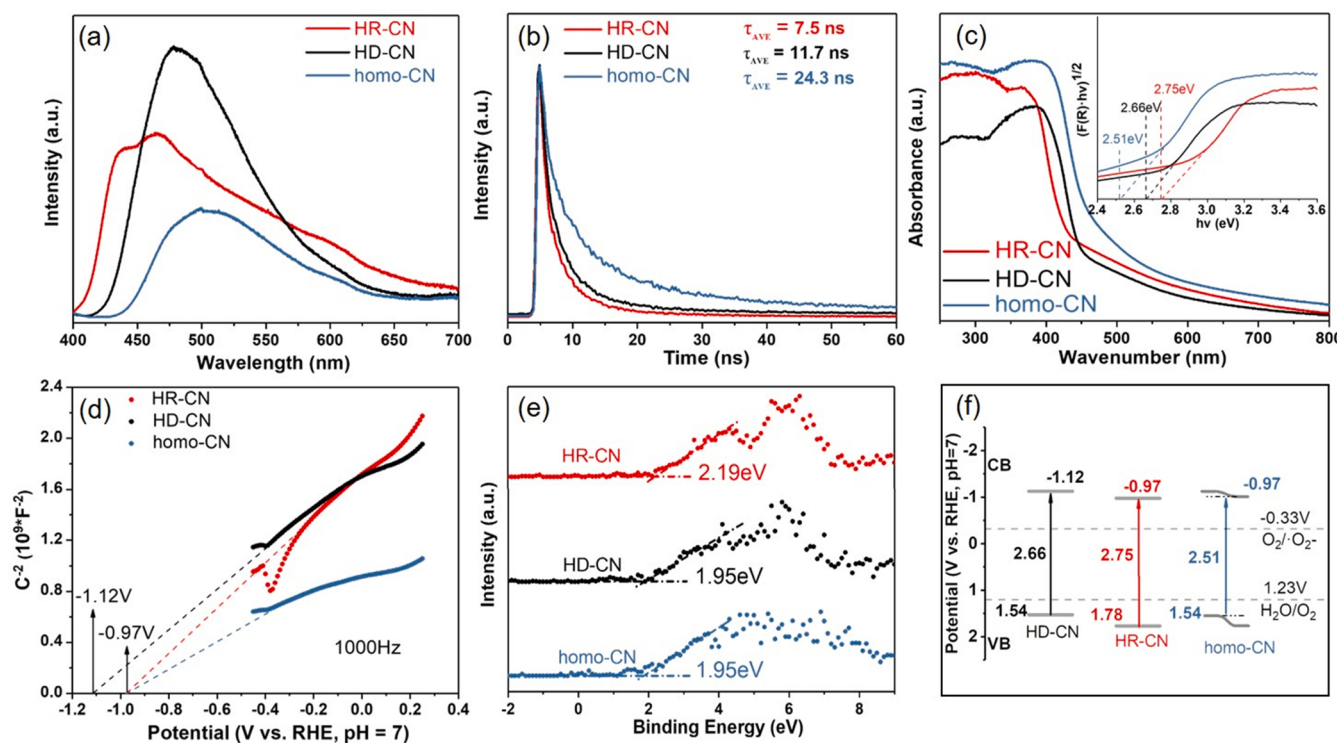


Fig. 3. (a) steady-state photoluminescence spectra and (b) fluorescence lifetime decay curves. (c) UV-vis DRS and energy band gap plots; (d) Mott-Schottky plots, (e) XPS valence band spectrum and (f) band structure alignments of HD-CN, HR-CN and homo-CN.

$\text{HD-CN} < \text{HR-CN} < \text{homo-CN}$ , manifest that the addition of HR-CN improves the charge transfer due to efficient charge separation by hydroxyl-induced homojunction.

### 3.4. Electron extraction induced charge separation due to hydroxyls on surface of homojunction

To understand the function of hydroxyl on  $\text{H}_2\text{O}_2$  formation, DFT simulation was performed on CN models terminated by either  $-\text{NH}_2$  or  $-\text{OH}$ . In Fig. 4a, a single-layer fragment with three tri-triazine units is adopted, in order to highlight the influence of terminations on the electronic properties of CN. With the evaluation of atomic circumstances, two carbon species together with three nitrogen species can be determined in each tri-triazine unit, labeled as  $\text{C}_1\text{-C}_2$  and  $\text{N}_1\text{-N}_3$  in the diagram, respectively. Fig. 4b illustrates the difference charge density map around terminations. While the covalent bond of  $\text{C}_2\text{-T}$  ( $\text{T} = \text{N}$  of  $-\text{NH}_2$ ,  $\text{O}$  of  $-\text{OH}$ ) in  $\text{g-C}_3\text{N}_4\text{-OH}$  turns out to be stronger than that in  $\text{g-C}_3\text{N}_4\text{-NH}_2$ , the charge transfer at  $\text{N}_2$  atom in these two models is close, indicating that the termination poses short range impacts on the electronic properties of CN generally localized to the  $\text{C}_2\text{-T}$  bond. A clear comparison of the band structures of  $\text{g-C}_3\text{N}_4\text{-NH}_2$  and  $\text{g-C}_3\text{N}_4\text{-OH}$  can be found in Fig. 4c. It can be clearly seen that the Fermi level is located at the valence band side, which is consistent with the reported features of  $\text{g-C}_3\text{N}_4$  monolayer. Fig. 4d shows the density of states (DOS) of  $\text{g-C}_3\text{N}_4\text{-NH}_2$  and  $\text{g-C}_3\text{N}_4\text{-OH}$ , with the specified contribution from each element (partial density of states, PDOS) calculated and displayed by dash lines. The position as well as the intensity of the peaks around Fermi level ( $-6 \text{ eV} \sim 2 \text{ eV}$ ) generally remains unchanged with the alternation of  $-\text{NH}_2$  by  $-\text{OH}$ , indicating that the termination poses limited impacts on the  $\pi$  bond from  $\text{Cp-Np}$  hybridization. Moreover, the bandgap of the two

studied models shares similar features: the valence band maximum (VBM) is composed of  $\text{Np}$  orbitals, while the conduction band minimum (CBM) is located at around 2 eV above. Fig. 4e demonstrates the composition of VBM and CBM of  $\text{g-C}_3\text{N}_4\text{-NH}_2$  (top) and  $\text{g-C}_3\text{N}_4\text{-OH}$  (down). It is revealed that the VBM in both two models are composed of  $\text{Np}$  orbitals from atom far from terminations. Consequently, the VBM of  $\text{g-C}_3\text{N}_4\text{-NH}_2$  and  $\text{g-C}_3\text{N}_4\text{-OH}$  are located at the same position. When it comes to the CBM, both contributions from  $\text{Cp-Np}$  and  $\text{C}_2\text{p-Tp}$  can be determined, in which the latter one makes a difference to the CBs of  $\text{g-C}_3\text{N}_4\text{-NH}_2$  and  $\text{g-C}_3\text{N}_4\text{-OH}$ : the peak intensity of  $\text{C}_2\text{p}$  in  $\text{g-C}_3\text{N}_4\text{-OH}$  is larger than that in  $\text{g-C}_3\text{N}_4\text{-NH}_2$ , making it capable of accommodating more excited electrons. In addition, the  $\text{Op}$  orbital in  $\text{g-C}_3\text{N}_4\text{-OH}$  is found to be located below the CB of  $\text{Cp-Np}$ , while the nitrogen of  $-\text{NH}_2$  donates its  $\text{Np}$  orbital to the CB at the similar position of  $\text{Cp-Np}$  in  $\text{g-C}_3\text{N}_4\text{-NH}_2$ . As a consequence, the presence of  $\text{Cp-Op}$  (of  $-\text{OH}$ ) hybridization below  $\text{Cp-Np}$  (of  $\text{g-C}_3\text{N}_4$ ) at CBM acts as shallow electron trap states in the  $\text{g-C}_3\text{N}_4\text{-OH}$ , extracting photoelectrons from the bulk to the surface. Therefore, accommodating excited electrons by hydroxyl-induced states facilitated spatial charge separation, which is mainly responsible for the efficient generation of  $\text{H}_2\text{O}_2$  [51,52]. Above analysis explains the negative SPV that we observed in Fig. 1 f well.

### 3.5. Improved kinetics for $\text{H}_2\text{O}_2$ generation and decomposition on hydroxyls

Since the formation and decomposition of  $\text{H}_2\text{O}_2$  will occur simultaneously during the photocatalytic process, a widely used equation (Eq. 5) for quantitatively analyzing the formation and decomposition rate of  $\text{H}_2\text{O}_2$  [41,53] is used for dynamic fitting of data in Fig. 2a:

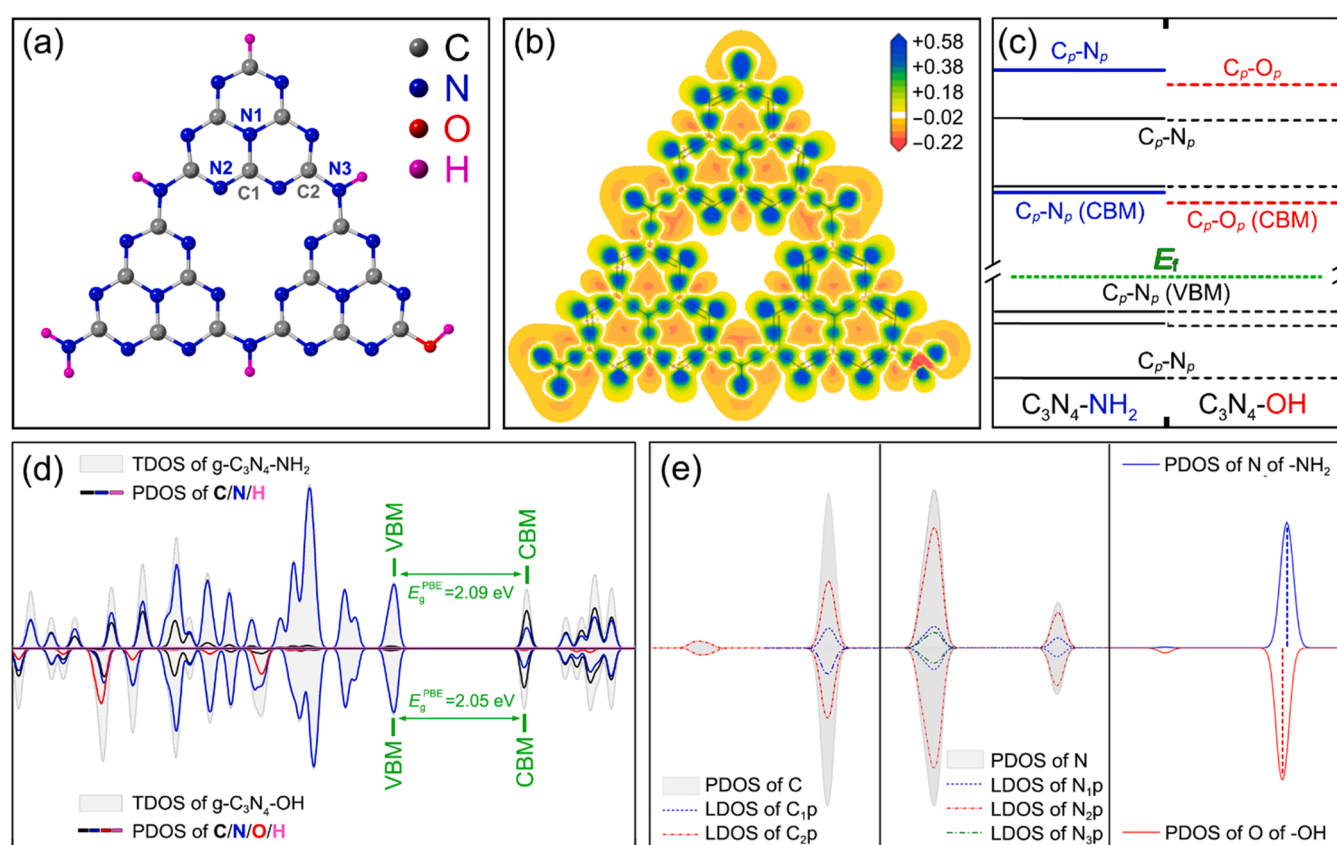


**Fig. 4.** (a) simulated models of  $\text{g-C}_3\text{N}_4$  nanosheet with terminations of  $-\text{NH}_2$  and  $-\text{OH}$ ; (b) difference charge density showing the electrons exchange effect around terminations; (c) refined band structure of  $\text{g-C}_3\text{N}_4\text{-NH}_2$  and  $\text{g-C}_3\text{N}_4\text{-OH}$  around Fermi level; (d) density of states curves of  $\text{g-C}_3\text{N}_4\text{-NH}_2$  and  $\text{g-C}_3\text{N}_4\text{-OH}$ ; (e) composition analysis of the valence band maximum (VBM) and conduction band minimum (CBM).

$$H_2O_2 = \frac{K_f}{K_d}(1 - \exp(-K_d \bullet t)) \quad (5)$$

The formation constant ( $K_f$ ) and decomposition constant ( $K_d$ ) of  $H_2O_2$  are calculated by zero-order and first-order kinetics and are exhibited in Fig. 5a. It can be found that the  $K_f$  of samples is in the order of homo-CN ( $11.99 \mu\text{M} \cdot \text{min}^{-1}$ ) > HD-CN ( $6.7 \mu\text{M} \cdot \text{min}^{-1}$ ) > HR-CN ( $1.86 \mu\text{M} \cdot \text{min}^{-1}$ ). Meanwhile, the  $K_d$  of homo-CN is dropped to  $1.28 \times 10^{-2} \text{ min}^{-1}$ , 3-time slower than that of HD-CN ( $3.4 \times 10^{-2} \text{ min}^{-1}$ ) and slightly higher than that of HR-CN ( $1.24 \times 10^{-2} \text{ min}^{-1}$ ). As a result, the value of  $K_d/K_f$  of homo-CN is the lowest ( $1.07 \times 10^{-3} \mu\text{M}^{-1}$ ), representing its suppressed surface back reaction referencing to its  $H_2O_2$  evolution rate, that is 6 times more efficient than HR-CN ( $6.67 \times 10^{-3} \mu\text{M}^{-1}$ ) and about 5 times more efficient than HD-CN ( $5.07 \times 10^{-3} \mu\text{M}^{-1}$ ). To further confirm the decomposition behavior of  $H_2O_2$  in the presence of photocatalysts, the  $H_2O_2$  decomposition experiments are measured with an initial  $H_2O_2$  concentration of  $2 \text{ mmol L}^{-1}$ . As shown in Fig. 5b, the  $H_2O_2$  concentration decreases by 22 % for homo-CN after 120 min irradiation under visible light without any sacrificial agent, which is lower than that for HD-CN (34 %). These results further confirm the inhibition of  $H_2O_2$  decomposition in the homo-CN, which will elevate the yield of  $H_2O_2$  production. According to the results of FTIR, XPS and NMR, the main difference between HD-CN and homo-CN or HR-CN is the amount of surface hydroxyl groups. Thus, it can be concluded that the surface hydroxyl groups probably inhibit the decomposition of  $H_2O_2$ .

DFT simulation is performed for both  $2e^-$  and  $4e^-$  ORR pathways to explicitly explain the rationale behind the inhibited back reaction of hydroxyl-rich surface for  $H_2O_2$  decomposition. Fig. 5c shows the absorption energy difference  $\Delta E_{\text{absorption}}$  of possible radicals ( $^*{\text{HOOH}}$ ,  $^*{\text{OH}}$ ,  $^*{\text{O}}$  and  $^*{\text{OOH}}$ ) on the surface g-C<sub>3</sub>N<sub>4</sub>-NH<sub>2</sub> and g-C<sub>3</sub>N<sub>4</sub>-OH. It can be seen that g-C<sub>3</sub>N<sub>4</sub>-OH exhibited stronger adsorption energy for  $^*{\text{OOH}}$  (the

intermediate species to form the final products of  $H_2O_2$ ), which decreases the selectivity of reaction for  $H_2O$  production. Fig. 5d illustrates the free energy diagrams of  $4e^-$  ORR pathways. Both g-C<sub>3</sub>N<sub>4</sub>-NH<sub>2</sub> and g-C<sub>3</sub>N<sub>4</sub>-OH tend to form  $H_2O_2$  (green line, at 3.52 eV eV) instead of  $^*{\text{O}}$  due to the lower Gibbs free energy. Nevertheless, the potential-determining step (PDS) for the  $4e^-$  ORR pathways of both two materials is found to be the transformation of  $^*{\text{OH}}$  to  $H_2O$ , as shown in Fig. 5e, that of g-C<sub>3</sub>N<sub>4</sub>-OH (1.04 eV) is higher than that of pristine g-C<sub>3</sub>N<sub>4</sub>-NH<sub>2</sub> (0.9 eV), making it reasonable to deduce that the alternation of  $^*{\text{NH}_2}$  by  $^*{\text{OH}}$  may hamper the  $4e^-$  ORR kinetics of g-C<sub>3</sub>N<sub>4</sub>. The decomposition of  $H_2O_2$  is evaluated by calculating the  $2e^-$  ORR pathways at the bias of  $U = 1.76 \text{ eV}$ , considering the decomposition of  $H_2O_2$  to  $H_2O$  through the radical of  $^*{\text{OH}}$ , as displayed in Fig. 5f. The overpotential for  $H_2O_2$  decomposition of g-C<sub>3</sub>N<sub>4</sub>-OH is higher than that of g-C<sub>3</sub>N<sub>4</sub>-NH<sub>2</sub>, with the values measured to be 0.51 eV and 0.37 eV, respectively, which is in well consistency with suppressed  $H_2O_2$  decomposition on CN with hydroxyl-rich surface.

According to the above analysis, Fig. 6 summarizes the mechanism for homo-CN to enhance the photocatalytic production of  $H_2O_2$ . When the CN homojunction is exposed to visible light, a built-in electric field generated at homojunction interface impels the electrons formed on the CB of HD-CN to transfer to the CB of HR-CN while the photo-generated holes of HR-CN migrating to the VB of HD-CN. The extra driving force for carrier transport caused by the potential difference between HD-CN and HR-CN (0.15 V for the conduction band and 0.24 V for the valence band) makes photo-generated electrons congregate in surface HR-CN and photo-generated holes transfer to bulk HD-CN, consequently reducing the recombination rate of electron-hole pairs. Additionally, the abundant hydroxyl groups in surface HR-CN nanolayer provide additional excited-electron accommodation bands for efficient electron extraction from the bulk to the surface. Meanwhile, hydroxyl groups enhance absorption energy of  $^*{\text{OOH}}$  and increase the overpotential for

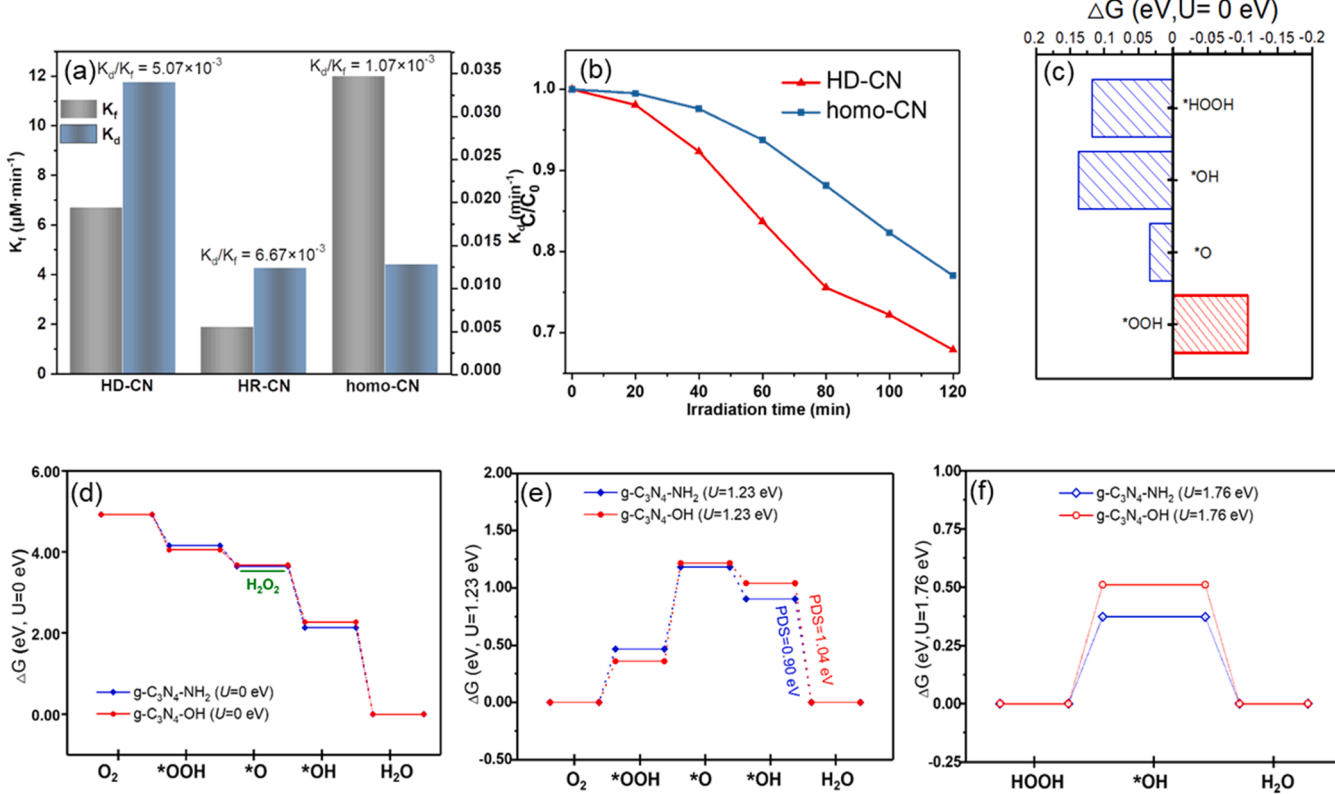
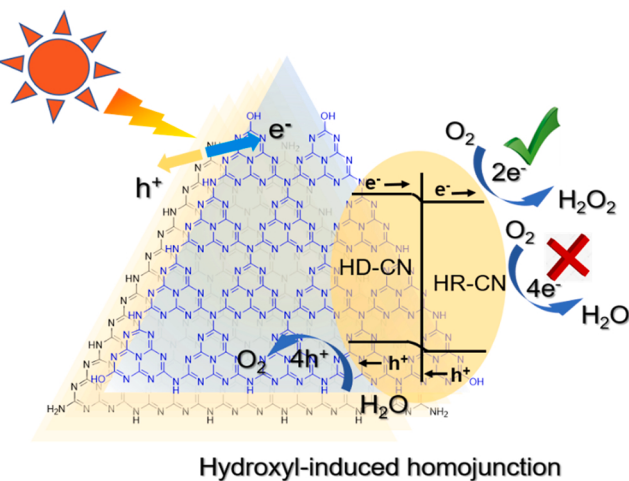


Fig. 5. (a)  $H_2O_2$  formation and decomposition constants derived from Fig. 2a; (b) the photocatalytic decomposition of  $H_2O_2$  ( $2 \text{ mmol L}^{-1}$ ) without sacrificial agent under visible light irradiation; (c) absorption energy difference of radicals on g-C<sub>3</sub>N<sub>4</sub>-NH<sub>2</sub> and g-C<sub>3</sub>N<sub>4</sub>-OH ( $\Delta G_{\text{g-C}_3\text{N}_4\text{-NH}_2} - \Delta G_{\text{g-C}_3\text{N}_4\text{-OH}}$ ); (d) calculated free energy of  $4e^-$  ORR steps; (e)  $4e^-$  ORR steps at the bias of  $1.23 \text{ eV}$ ; (f)  $2e^-$  ORR steps at the bias of  $1.76 \text{ eV}$ .



**Fig. 6.** Mechanism for the improved photocatalytic  $\text{H}_2\text{O}_2$  generation over the hydroxyl-induced homojunction.

4-electron reduction reaction of  $\text{O}_2$ , thus inhibit the decomposition of as-generated  $\text{H}_2\text{O}_2$ . Combining above advantages, our CN homojunction obtains an efficient photocatalytic production of  $\text{H}_2\text{O}_2$  under visible light.

#### 4. Conclusion

In summary, this work constructs a hydroxyl-induced CN homojunction (homo-CN) with the functional surface by enclosing hydroxyl-deficient CN nanosheets with hydroxyl-rich CN topping layer. The variation in hydroxyl concentration on CN samples tuned their band structures, forming a gradient driving force for electron-hole separation. Kinetically, surface hydroxyls provide extra electron accommodation bands for efficient electron extraction from the bulk to the surface which are visually observed with a KPFM and rationalized by DFT calculations. Meanwhile, surface hydroxyls suppress  $\text{H}_2\text{O}_2$  back reaction on surface by enhancing the absorption energy of  $^{\bullet}\text{OOH}$  (the intermediate species to form the final products of  $\text{H}_2\text{O}_2$ ) and increasing the overpotential for the 4e<sup>-</sup> ORR. As a result, homo-CN possesses a photocatalytic  $\text{H}_2\text{O}_2$  production rate 4.5 times higher than bulk CN; and a high AQY of 2.1 % at 500 nm without any sacrificial agent. This work demonstrates a strategy for coping with the detrimental  $\text{H}_2\text{O}_2$  back reaction on a homojunction to achieve favorable surface kinetics and spatial charge separation simultaneously. This study is meaningful for dealing with the bottleneck (back reaction of accumulated  $\text{H}_2\text{O}_2$ ) of efficient, longtime and large-scale  $\text{H}_2\text{O}_2$  photosynthesis.

#### CRediT authorship contribution statement

**Qichao Chen:** Methodology, Data curation, Writing – original draft. **Chengjie Lu:** Data curation, Methodology, Investigation, Software, Validation. **Boyu Ping:** Resources, Editing. **Guiyang Li:** Resources, Software. **Jiayi Chen:** Resources, Software. **ZhengMing Sun:** Methodology. **Yuanjian Zhang:** Methodology. **Li Tao:** Project administration, Funding acquisition, Supervision. **Qiusi Ruan:** Project administration, Funding acquisition, Review, Supervision.

#### Declaration of Competing Interest

The authors declare that they have no known competing financial interests or personal relationships that could have appeared to influence the work reported in this paper.

#### Data availability

Data will be made available on request.

#### Acknowledgements

This work was supported by the National Natural Science Foundation of China (92164102) and (2210020499), Jiangsu Province Innovation Talent Program, Jiangsu Province Six-Category Talent Program (Grant DZXX-011), and Fundamental Research Funds for the Central Universities (2242022k30008).

#### Appendix A. Supporting information

Supplementary data associated with this article can be found in the online version at doi:10.1016/j.apcatb.2022.122216.

#### References

- [1] H. Yu, Q. Zhang, H. Liu, M. Dahl, J.B. Joo, N. Li, L. Wang, Y. Yin, Thermal synthesis of silver nanoplates revisited: a modified photochemical process, *ACS Nano* 8 (2014) 10252–10261.
- [2] J.G. Barbosa, F. Benetti, M. De Oliveira Gallinari, M. Carminatti, A.B.D. Da Silva, I. N.I. Lopes, A.L.F. Briso, L.T.A. Cintra, Bleaching gel mixed with MI Paste Plus reduces penetration of  $\text{H}_2\text{O}_2$  and damage to pulp tissue and maintains bleaching effectiveness, *Clin. Oral. Investig.* 24 (2020) 1299–1309.
- [3] C.J. McDonnell-Worth, D.R. MacFarlane, Progress towards direct hydrogen peroxide fuel cells (DHPFCs) as an energy storage concept, *Aust. J. Chem.* 71 (2018) 781–788.
- [4] H. Hou, X. Zeng, X. Zhang, Production of hydrogen peroxide by photocatalytic processes, *Angew. Chem. Int. Ed.* 59 (2020) 17356–17376.
- [5] H. Hirakawa, S. Shiota, Y. Shiraishi, H. Sakamoto, S. Ichikawa, T. Hirai, Au nanoparticles supported on  $\text{BiVO}_4$ : effective inorganic photocatalysts for  $\text{H}_2\text{O}_2$  production from water and  $\text{O}_2$  under visible light, *ACS Catal.* 6 (2016) 4976–4982.
- [6] X. Meng, P. Zong, L. Wang, F. Yang, W. Hou, S. Zhang, B. Li, Z. Guo, S. Liu, G. Zuo, Y. Du, T. Wang, V.A.L. Roy, Au-nanoparticle-supported  $\text{ZnO}$  as highly efficient photocatalyst for  $\text{H}_2\text{O}_2$  production, *Catal. Commun.* 134 (2020).
- [7] H. Song, L. Wei, L. Chen, H. Zhang, J. Su, Photocatalytic production of hydrogen peroxide over modified semiconductor materials: a minireview, *Top. Catal.* 63 (2020) 895–912.
- [8] L. Feng, B. Li, Y. Xiao, L. Li, Y. Zhang, Q. Zhao, G. Zuo, X. Meng, V.A.L. Roy, Au modified  $\text{Bi}_2\text{O}_3\text{-TiO}_2$  hybrid for photocatalytic synthesis of hydrogen peroxide, *Catal. Commun.* 155 (2021).
- [9] M. Nagamitsu, K. Awa, H. Tada, Hydrogen peroxide synthesis from water and oxygen using a three-component nanohybrid photocatalyst consisting of Au particle-loaded rutile  $\text{TiO}_2$  and  $\text{RuO}_2$  with a heteroepitaxial junction, *Chem. Commun.* 56 (2020) 8190–8193.
- [10] P. Gundogmus, J. Park, A. Ozturk, Preparation and photocatalytic activity of  $\text{g-C}_3\text{N}_4\text{/TiO}_2$  heterojunctions under solar light illumination, *Ceram. Int.* 46 (2020) 21431–21438.
- [11] M. Xu, Y. Zhu, J. Yang, W. Li, C. Sun, Y. Cui, L. Liu, H. Zhao, B. Liang, Enhanced interfacial electronic transfer of  $\text{BiVO}_4$  coupled with 2D  $\text{g-C}_3\text{N}_4$  for visible-light photocatalytic performance, *J. Am. Ceram. Soc.* 104 (2021) 3004–3018.
- [12] Z. Sun, H. Wang, Z. Wu, L. Wang,  $\text{g-C}_3\text{N}_4$  based composite photocatalysts for photocatalytic  $\text{CO}_2$  reduction, *Catal. Today* 300 (2018) 160–172.
- [13] W. Yu, D. Xu, T. Peng, Enhanced photocatalytic activity of  $\text{g-C}_3\text{N}_4$  for selective  $\text{CO}_2$  reduction to  $\text{CH}_3\text{OH}$  via facile coupling of  $\text{ZnO}$ : a direct Z-scheme mechanism, *J. Mater. Chem. A* 3 (2015) 19936–19947.
- [14] Y. Shiraishi, S. Kanazawa, Y. Sugano, D. Tsukamoto, H. Sakamoto, S. Ichikawa, T. Hirai, Highly selective production of hydrogen peroxide on graphitic carbon nitride ( $\text{g-C}_3\text{N}_4$ ) photocatalyst activated by visible light, *ACS Catal.* 4 (2014) 774–780.
- [15] Y. Shiraishi, Y. Kofuji, H. Sakamoto, S. Tanaka, S. Ichikawa, T. Hirai, Effects of surface defects on photocatalytic  $\text{H}_2\text{O}_2$  production by mesoporous graphitic carbon nitride under visible light irradiation, *ACS Catal.* 5 (2015) 3058–3066.
- [16] P. Zhang, Y. Tong, Y. Liu, J.J.M. Vequizo, H. Sun, C. Yang, A. Yamakata, F. Fan, W. Lin, X. Wang, W. Choi, Heteroatom dopants promote two-electron  $\text{O}_2$  reduction for photocatalytic production of  $\text{H}_2\text{O}_2$  on polymeric carbon nitride, *Angew. Chem. Int. Ed.* 59 (2020) 16209–16217.
- [17] Z. Teng, Q. Zhang, H. Yang, K. Kato, W. Yang, Y.-R. Lu, S. Liu, C. Wang, A. Yamakata, C. Su, B. Liu, T. Ohno, Atomically dispersed antimony on carbon nitride for the artificial photosynthesis of hydrogen peroxide, *Nat. Catal.* 4 (2021) 374–384.
- [18] X. Li, J. Zhang, F. Zhou, H. Zhang, J. Bai, Y. Wang, H. Wang, Preparation of N-vacancy-doped  $\text{g-C}_3\text{N}_4$  with outstanding photocatalytic  $\text{H}_2\text{O}_2$  production ability by dielectric barrier discharge plasma treatment, *Chin. J. Catal.* 39 (2018) 1090–1098.
- [19] L. Shi, L. Yang, W. Zhou, Y. Liu, L. Yin, X. Hai, H. Song, J. Ye, Photoassisted construction of Holey defective  $\text{g-C}_3\text{N}_4$  photocatalysts for efficient visible-light-driven  $\text{H}_2\text{O}_2$  production, *Small* 14 (2018).

[20] X. Chang, J. Yang, D. Han, B. Zhang, X. Xiang, J. He, Enhancing light-driven production of hydrogen peroxide by anchoring Au onto  $\text{C}_3\text{N}_4$  catalysts, *Catalysts* 8 (2018).

[21] J. Cai, J. Huang, S. Wang, J. Iocozzia, Z. Sun, J. Sun, Y. Yang, Y. Lai, Z. Lin, Crafting Mussel-inspired metal nanoparticle-decorated ultrathin graphitic carbon nitride for the degradation of chemical pollutants and production of chemical resources, *Adv. Mater.* 31 (2019).

[22] Z. Li, N. Xiong, G. Gu, Fabrication of a full-spectrum-response  $\text{Cu}_2(\text{OH})_2\text{CO}_3/\text{g-C}_3\text{N}_4$  heterojunction catalyst with outstanding photocatalytic  $\text{H}_2\text{O}_2$  production performance via a self-sacrificial method, *Dalton Trans.* 48 (2019) 182–189.

[23] Y. Shan, Y. Guo, Y. Wang, X. Du, J. Yu, H. Luo, H. Wu, B. Boury, H. Xiao, L. Huang, L. Chen, Nanocellulose-derived carbon/ $\text{g-C}_3\text{N}_4$  heterojunction with a hybrid electron transfer pathway for highly photocatalytic hydrogen peroxide production, *J. Colloid Interface Sci.* 599 (2021) 507–518.

[24] Y. Yang, C. Zhang, D. Huang, G. Zeng, J. Huang, C. Lai, C. Zhou, W. Wang, H. Guo, W. Xue, R. Deng, M. Cheng, W. Xiong, Boron nitride quantum dots decorated ultrathin porous  $\text{g-C}_3\text{N}_4$ : intensified exciton dissociation and charge transfer for promoting visible-light-driven molecular oxygen activation, *Appl. Catal. B Environ.* 245 (2019) 87–99.

[25] Q. Liang, Z. Li, Y. Bai, Z.-H. Huang, F. Kang, Q.-H. Yang, A. Composite, Polymeric carbon nitride with in situ formed isotype heterojunctions for highly improved photocatalysis under visible light, *Small* 13 (2017).

[26] P. Ma, X. Zhang, C. Wang, Z. Wang, K. Wang, Y. Feng, J. Wang, Y. Zhai, J. Deng, L. Wang, K. Zheng, Band alignment of homojunction by anchoring CN quantum dots on  $\text{g-C}_3\text{N}_4$  (OD/2D) enhance photocatalytic hydrogen peroxide evolution, *Appl. Catal. B Environ.* 300 (2022).

[27] Q. Deng, H. Li, G. Ba, T. Huo, W. Hou, The pivotal role of defects in fabrication of polymeric carbon nitride homojunctions with enhanced photocatalytic hydrogen evolution, *J. Colloid Interface Sci.* 586 (2021) 748–757.

[28] H. Dong, X. Zhang, J. Li, P. Zhou, S. Yu, N. Song, C. Liu, G. Che, C. Li, Construction of morphology-controlled nonmetal 2D/3D homojunction towards enhancing photocatalytic activity and mechanism insight, *Appl. Catal. B Environ.* 263 (2020).

[29] J. Cao, C. Pan, Y. Ding, W. Li, K. Lv, H. Tang, Constructing nitrogen vacancy introduced  $\text{g-C}_3\text{N}_4$  p-n homojunction for enhanced photocatalytic activity, *J. Environ. Chem. Eng.* 7 (2019).

[30] H. Sun, C. Neumann, T. Zhang, M. Löffler, A. Wolf, Y. Hou, A. Turchanin, J. Zhang, X. Feng, Poly(1,4-Diethynylbenzene) gradient homojunction with enhanced charge carrier separation for photoelectrochemical water reduction, *Adv. Mater.* 31 (2019), e1900961.

[31] Z. Ai, K. Zhang, D. Shi, B. Chang, Y. Shao, L. Zhang, Y. Wu, X. Hao, Band-matching transformation between  $\text{CdS}$  and BCNNTs with tunable p-n homojunction for enhanced photocatalytic pure water splitting, *Nano Energy* 69 (2020).

[32] L. Zhou, J. Lei, F. Wang, L. Wang, M.R. Hoffmann, Y. Liu, S.-I. In, J. Zhang, Carbon nitride nanotubes with in situ grafted hydroxyl groups for highly efficient spontaneous  $\text{H}_2\text{O}_2$  production, *Appl. Catal. B Environ.* 288 (2021).

[33] H. Che, X. Gao, J. Chen, J. Hou, Y. Ao, P. Wang, Iodide-induced fragmentation of polymerized hydrophilic carbon nitride for high-performance quasi-homogeneous photocatalytic  $\text{H}_2\text{O}_2$  production, *Angew. Chem. Int. Ed.* 60 (2021) 25546–25550.

[34] M. Wu, Y. Gong, T. Nie, J. Zhang, R. Wang, H. Wang, B. He, Template-free synthesis of nanocage-like  $\text{g-C}_3\text{N}_4$  with high surface area and nitrogen defects for enhanced photocatalytic  $\text{H}_2$  activity, *J. Mater. Chem. A* 7 (2019) 5324–5332.

[35] X. Qiao, Z. Zhou, X. Liu, C. Zhao, Q. Guan, W. Li, Constructing a fragmentary  $\text{g-C}_3\text{N}_4$  framework with rich nitrogen defects as a highly efficient metal-free catalyst for acetylene hydrochlorination, *Catal. Sci. Technol.* 9 (2019) 3753–3762.

[36] N.D. Shcherban, P. Maki-Arvela, A. Aho, S.A. Sergienko, P.S. Yaremov, K. Eranen, D.Y. Murzin, Melamine-derived graphitic carbon nitride as a new effective metal-free catalyst for Knoevenagel condensation of benzaldehyde with ethylcyanoacetate, *Catal. Sci. Technol.* 8 (2018) 2928–2937.

[37] X. Wang, K. Maeda, A. Thomas, K. Takanabe, G. Xin, J.M. Carlsson, K. Domen, M. Antonietti, A metal-free polymeric photocatalyst for hydrogen production from water under visible light, *Nat. Mater.* 8 (2009) 76–80.

[38] B. Babu, J. Shim, A.N. Kadam, K. Yoo, Modification of porous  $\text{g-C}_3\text{N}_4$  nanosheets for enhanced photocatalytic activity: in-situ synthesis and optimization of  $\text{NH}_4\text{Cl}$  quantity, *Catal. Commun.* 124 (2019) 123–127.

[39] L. Wang, G. Zhou, Y. Tian, L. Yan, M. Deng, B. Yang, Z. Kang, H. Sun, Hydroxyl decorated  $\text{g-C}_3\text{N}_4$  nanoparticles with narrowed bandgap for high efficient photocatalyst design, *Appl. Catal. B Environ.* 244 (2019) 262–271.

[40] Y. Liu, M. Zhang, Z. Wang, J. He, J. Zhang, S. Ye, X. Wang, D. Li, H. Yin, Q. Zhu, H. Jing, Y. Weng, F. Pan, R. Chen, C. Li, F. Fan, Bipolar charge collecting structure enables overall water splitting on ferroelectric photocatalysts, *Nat. Commun.* 13 (2022).

[41] Z. Haider, H.-i Cho, G.-h Moon, H.-i Kim, Minireview: selective production of hydrogen peroxide as a clean oxidant over structurally tailored carbon nitride photocatalysts, *Catal. Today* 335 (2019) 55–64.

[42] H. Xie, Y. Zheng, X. Guo, Y. Liu, Z. Zhang, J. Zhao, W. Zhang, Y. Wang, Y. Huang, Rapid microwave synthesis of mesoporous oxygen-doped  $\text{g-C}_3\text{N}_4$  with carbon vacancies for efficient photocatalytic  $\text{H}_2\text{O}_2$  production, *ACS Sustain. Chem. Eng.* 9 (2021) 6788–6798.

[43] J. Ma, X. Peng, Z. Zhou, H. Yang, K. Wu, Z. Fang, D. Han, Y. Fang, S. Liu, Y. Shen, Y. Zhang, Extended conjugation refining carbon nitride for non-sacrificial  $\text{H}_2\text{O}_2$  photosynthesis and hypoxic tumor therapy, *Angew. Chem. (Int. Ed. Engl.)* (2022).

[44] Y. Li, J. Xue, Q. Shen, S. Jia, Q. Li, Y. Li, X. Liu, H. Jia, Construction of a ternary spatial junction in yolk-shell nanoreactor for efficient photo-thermal catalytic hydrogen generation, *Chem. Eng. J.* 423 (2021).

[45] G. Zhang, G. Li, Z.-A. Lan, L. Lin, A. Savateev, T. Heil, S. Zafeiratos, X. Wang, M. Antonietti, Optimizing optical absorption, exciton dissociation, and charge transfer of a polymeric carbon nitride with ultrahigh solar hydrogen production activity, *Angew. Chem. Int. Ed.* 56 (2017) 13445–13449.

[46] C. Feng, L. Tang, Y. Deng, J. Wang, J. Luo, Y. Liu, X. Ouyang, H. Yang, J. Yu, J. Wang, Synthesis of leaf-vein-Like  $\text{g-C}_3\text{N}_4$  with tunable band structures and charge transfer properties for selective photocatalytic  $\text{H}_2\text{O}_2$  evolution, *Adv. Funct. Mater.* 30 (2020).

[47] G. Liu, G. Zhao, W. Zhou, Y. Liu, H. Pang, H. Zhang, D. Hao, X. Meng, P. Li, T. Kako, J. Ye, In situ bond modulation of graphitic carbon nitride to construct p-n homojunctions for enhanced photocatalytic hydrogen production, *Adv. Funct. Mater.* 26 (2016) 6822–6829.

[48] J. Lyu, J. Gao, M. Zhang, Q. Fu, L. Sun, S. Hu, J. Zhong, S. Wang, J. Li, Construction of homojunction-adsorption layer on anatase  $\text{TiO}_2$  to improve photocatalytic mineralization of volatile organic compounds, *Appl. Catal. B Environ.* 202 (2017) 664–670.

[49] C. Yang, S. Wan, B. Zhu, J. Yu, S. Cao, Calcination-regulated microstructures of donor-acceptor polymers towards enhanced and stable photocatalytic  $\text{H}_2\text{O}_2$  production in pure water, *Angew. Chem. Int. Ed.* 61 (2022).

[50] C. Li, G. Chen, J. Sun, J. Rao, Z. Han, Y. Hu, W. Xing, C. Zhang, Doping effect of phosphate in  $\text{Bi}_2\text{WO}_6$  and universal improved photocatalytic activity for removing various pollutants in water, *Appl. Catal. B Environ.* 188 (2016) 39–47.

[51] J.H. Lee, H. Cho, S.O. Park, J.M. Hwang, Y. Hong, P. Sharma, W.C. Jeon, Y. Cho, C. Yang, S.K. Kwak, H.R. Moon, J.-W. Jang, High performance  $\text{H}_2\text{O}_2$  production achieved by sulfur-doped carbon on  $\text{CdS}$  photocatalyst via inhibiting reverse  $\text{H}_2\text{O}_2$  decomposition, *Appl. Catal. B Environ.* 284 (2021).

[52] H.-i Kim, O.S. Kwon, S. Kim, W. Choi, J.-H. Kim, Harnessing low energy photons (635 nm) for the production of  $\text{H}_2\text{O}_2$  using upconversion nanohybrid photocatalysts, *Energy Environ. Sci.* 9 (2016) 1063–1073.

[53] Y. Yang, Z. Zeng, G. Zeng, D. Huang, R. Xiao, C. Zhang, C. Zhou, W. Xiong, W. Wang, M. Cheng, W. Xue, H. Guo, X. Tang, D. He,  $\text{Ti}_3\text{C}_2$  Mxene/porous  $\text{g-C}_3\text{N}_4$  interfacial Schottky junction for boosting spatial charge separation in photocatalytic  $\text{H}_2\text{O}_2$  production, *Appl. Catal. B Environ.* 258 (2019).